Supporting Information

D-Orbitals Modulation of High-Entropy Sulfides with Amorphous/Crystalline Heterostructures for Simultaneous Hydrogen Production and Sulfur Recovery

Ruotong Liu[a], Jingying Li[a], Yu Pang[a], Yanru Liu[a], Xiaolong Wang[a], Dan Zhang[b]*, Hongdong Li[a]* and Lei Wang[a]*

[a]Key Laboratory of Eco-Chemical Engineering, International Science and Technology Cooperation Base of Eco-Chemical Engineering and Green Manufacturing, College of Chemistry and Molecular Engineering, Qingdao University of Science and Technology, Qingdao 266042, P. R. China

[b]Key Laboratory of Catalytic Conversion and Clean Energy in Universities of Shandong Province, School of Chemistry and Chemical Engineering, Qufu Normal University, Qufu, Shandong 273165, PR China, P. R. China

Experimental Section

Chemicals and materials: Nickel foam (1.5 mm, thick1.5 mm, thick; 110 ppi pore size; ~97% porosity) was purchased from Suzhoukeshenghe Metal Materials Co., Ltd. (Suzhou, China). Cobalt chloride (II) ($CoCl_2·6H_2O$ ≥97%), Sodium hydroxide (NaOH, 96%) and Ruthenium oxide (RuO_2) got from Shanghai Macklin Biochemical Co., Ltd. Nickel chloride (II) ($NiCl_2·6H_2O$ ≥97%) and Sodium sulfide nonahydrate ($Na_2S·9H_2O$ ≥98%) was taken from Aladdin. Manganese chloride (II) ($MnCl_2·4H_2O$ ≥98%) was received from Sigma Aldrich (Shanghai) Trading Co., Ltd. Magnesium chloride (II) ($MgCl_2$ ≥98%) was received from Beijing Bailingwei Technology Co., Ltd. Hydrochloric acid (HCl ≥37%) was provided by Xilong Scientific Co., Ltd. Iron (II) sulfate heptahydrate ($FeSO_4·7H_2O$ ≥99%), Sodium thiosulfate pentahydrate ($Na_2S_2O_3·5H_2O$ ≥99%) and Ethanol (C_2H_6O ≥99.7%) were sourced from Sinopharm Chemical Reagent Co., Ltd. All chemicals are used without further purification. The deionized water in the experiment is ultrapure water (18.2 MΩ·cm).

Preparation of nickel foam: A 2×2 cm^2 of nickel foam (NF) was ultra-sounded with HCl (1 M), Milli-Q water, and ethanol maintaining 10 min, respectively, to ensure that there is no oxide and the other materials on the surface.

Preparation of FeCoNiMnMg-S: For FeCoNiMnMg-S, $Na_2S_2O_3·5H_2O$ (0.7 M) and $FeSO_4·7H_2O$ (0.2 M), $NiCl_2·6H_2O$ (0.2 M), $CoCl_2·6H_2O$ (0.2 M), $MnCl_2·4H_2O$ (0.2 M), $MgCl_2$ (0.2 M) was dissolved in 30 mL deionized water and stirred for 10 minutes at room temperature. Then a piece of Ni foam (2×2 cm^2) was put into the solution at 25 ºC and oscillating frequency of 150 rpm min^{-1} for 2 h to ensure that the surface of the NF can be completely reacted. After stirring, the prepared samples were rinsed

three times with deionized water. Finally, FeCoNiMnMg-S was obtained by vacuum drying in an oven at 60 ºC.

Preparation of FeCoNiMg-S: FeCoNiMg-S was synthesized in a similar way to FeCoNiMnMg-S. For FeCoNiMg-S, $Na_2S_2O_3 \cdot 5H_2O$ (0.7 M) and $FeSO_4 \cdot 7H_2O$ (0.2 M), $NiCl_2 \cdot 6H_2O$ (0.2 M), $CoCl_2 \cdot 6H_2O$ (0.2 M), $MgCl_2$ (0.2 M) was dissolved in 30 mL deionized water and stirred for 10 minutes at room temperature. After that, a piece of NF was put into the beaker. The reaction conditions are the same as those of FeCoNiMnMg-S. Afterwards, deionized water was served to wash the collected NF three times. Finally, FeCoNiMg-S was obtained by vacuum drying in an oven at 60 ºC.

Preparation of FeCoNi-S: FeCoNi-S was synthesized in a similar way to FeCoNiMnMg-S. For FeCoNi-S, $Na_2S_2O_3 \cdot 5H_2O$ (0.7 M) and $FeSO_4 \cdot 7H_2O$ (0.2 M), $NiCl_2 \cdot 6H_2O$ (0.2 M), $CoCl_2 \cdot 6H_2O$ (0.2 M) was dissolved in 30 mL deionized water and stirred for 10 minutes at room temperature. After that, a piece of NF was put into the beaker. The reaction conditions are the same as those of FeCoNiMnMg-S. Afterwards, deionized water was served to wash the collected NF three times. Finally, FeCoNi-S was obtained by vacuum drying in an oven at 60 ºC

Materials characterizations: For scanning electron microscope (SEM), the FeCoNiMnMg-S nanosheets grown on NF were cut into 0.5cm*0.5cm sheets and pasted on the sample stage, and the samples were tested on Hitachi Regulus 8100 instrument. For transmission electron microscopy (TEM) observation, the FeCoNiMnMg-S nanosheets grown on NF were immersed into ethanol and sonicated for 5 min. Then a few drops of the suspension were casted onto lacey carbon supported TEM grids. TEM was carried out on a FEI Tecnai-G2 F30 transmission electron microscope operated at an accelerating voltage of 200 kV. Powder X-ray diffraction (XRD) spectra were recorded on X'Pert-PRO MPD diffractometer

operating at 40 kV and 40 mA with Cu Kα radiation. In order to analyze the valence state of the catalyst by X-ray photoelectron spectroscopy (XPS), FeCoNiMnMg-S nanosheets grown on NF were sheared into 1 cm*1 cm sheet and then subjected to a monochromatic Al Kα source on an Axis Supra spectrometer at 15 mA and 14 kV. The spectrum was calibrated by carbon 1s spectrum, and its main line was set to 284.8 eV, and then the valence state of the catalyst was analyzed using CasaXPS software. Contact angles of water were evaluated by Dataphysics Contact Angel Tester. UV-visible spectrum was used to test the anodic products of polysulfides (Tianmei UV2600, 1 nm resolution, with deionised water as reference).

Electrochemical measurements: Electrochemical measurements were conducted on a CHI 660 (Shanghai Chenhua Instrument Corporation, China) / Gamry Reference 3000 Electrochemical Workstation in a conventional three-electrode cell by using a carbon rod as the counter electrode and a mercuric oxide electrode as the reference electrode. Meanwhile, high-entropy hydroxide nanosheets loaded on NF are directly used as working electrodes. The potentials were converted to the reversible hydrogen electrode (RHE) according to the following equation: E (RHE) = E (Hg/HgO) + 0.098 V + 0.0592 × pH. The OER performance of the catalysts was evaluated by linear sweep voltammetry (LSV) with a scan rate of 10 mV s^{-1} in 1.0 M NaOH and 1.0 M NaOH + 3.0 M Na_2S, and all polarization curves were 95% iR-corrected. EIS measurements were measured in the frequency range from 100 kHz to 0.1 Hz. The Tafel slope is obtained by fitting the linear portion of the Tafel curve to the equation [$\eta = b \log(j) + a$]. The durability test was performed in 1.0 M NaOH and 1.0 M NaOH + 3.0 M Na_2S using the chronoamperometric method. RuO_2 catalyst was also dropped on the Ni foam as a reference catalyst for electrochemical tests under the same conditions.

Calculation of electrochemical active surface area (ECSA): The double layer capacity (C_{dl}) is derived from the CV curves with different scanning rates (20, 40, 60, 80, 100 mV s^{-1}). The electrochemical active surface area (ECSA) of the catalyst was estimated by C_{dl}, the specific equation is as follows:

$$ECSA = \frac{C_{dl}}{C_s}$$

Here, Cs is the specific capacitance of the sample which is usually 0.04 mF cm^{-2}.

Calculation of turnover frequency (TOF)： The intrinsic catalytic activity is measured by the turnover frequency (TOF). We attempted to quantify the active sites by electrochemical methods. The intrinsic catalytic performance of each active site was revealed based on CV.

$$TOF(s^{-1}) = \frac{I}{zFn}$$

The I (A) is the current measured at a specific potential during LSV measurement, n is the number of surface active sites calculated using n = Q/zF, where Q is the absolute charge, and its value depends on the integral area of the time-dependent curve of the current versus RHE using CV scanning from –0.2 to 0.6 V in 1.0 M phosphate buffer solution (PBS) at pH = 7. z denotes the number of transferred electrons, F is the Faradic constant (96485 C mol^{-1}).

Calculation of SOR Faradic efficiency (FE): The mass of sulfur powder (mS) was obtained after acidification, centrifugation and drying, after each chronoamperometric tests. According to the following equation for calculating the relevant FE of SOR:

$$N_s = \frac{ms}{M_s}$$

$$FE = (Ns \times Z \times F)/Q \times 100\%$$

Where F is the Faraday constant (96485 C mol^{-1}), Z is the electron number transferred during the whole process of oxidation of S^{2-} to S (Z=2), Q is the recorded charge during the electrolysis, M_S is the relative molecular mass of S and N_S is the molar amount for S product.

Recycling Sulfur Powder Derived from Oxidation Products: The H_2SO_4 solution was added drop by drop into the electrolyte after SOR until the pH reached 1 in an ice bath. The sulfur precipitated as yellow products and was separated by filtration.

Density functional theory (DFT) calculation:

The density functional theory (DFT) calculations were performed using the Vienna Ab initio Simulation Package (VASP).[1, 2] The exchange-correlation functional was treated within the generalized gradient approximation (GGA) as parameterized by Perdew-Burke-Ernzerhof (PBE).[3, 4] The projector augmented-wave (PAW) method was employed to describe the ionic cores, and the valence electrons were expanded in a plane-wave basis set with a kinetic energy cutoff of 520 eV. To construct the interfacial architecture of the high-entropy sulfide, a sophisticated crystalline-non-crystalline heterostructured model was systematically developed through the implementation of ab initio molecular dynamics (AIMD) simulations. The modeling strategy involved a spatially constrained approach, wherein the atomic coordinates of exactly one-half of the computational supercell were maintained in a rigidly fixed state to preserve the structural integrity and long-range order of the crystalline lattice. Concurrently, the unconstrained region of the ensemble was subjected to thermal evolution within the canonical (NVT) ensemble. To ensure sufficient phase transition

and the attainment of a representative disordered state, the simulation was equilibrated at an elevated temperature of 1500 K over an extensive temporal duration of 1000 fs. The numerical integration of the atomic trajectories was executed with a refined temporal resolution, utilizing a consistent time step of 1 fs to capture the delicate structural dynamics at the hetero-interface. During the static calculations, a Γ-centered 1×1×1 k point mesh was adopted for structural optimization of the bulk and surface models, while a 3×3×1 mesh was used for density of states analysis. Electronic relaxation was considered converged when the total energy change fell below 10^{-7} eV, and geometric optimization was deemed complete when the forces on all atoms were less than 0.02 eV $Å^{-1}$. Van der Waals interactions were accounted for using the Grimme DFT D3 dispersion correction scheme. The Gibbs free energy was evaluated as follows:

$$\Delta E_{ads} = \mathrm{E(slab + ads) - E(slab) - E(ads)}$$

$$\Delta G_{ads} = \Delta E_{ads} - \Delta \mathrm{ZPE} - \mathrm{T}\Delta S$$

Among them, $\Delta G_{ads}$is the free energy difference before and after adsorption, $\Delta E_{ads}$is the DFT energy difference before and after adsorption, ΔZPE is the zero point energy difference before and after adsorption, and ΔS is the entropy difference before and after adsorption. All calculation were spin-polarized.

Figures

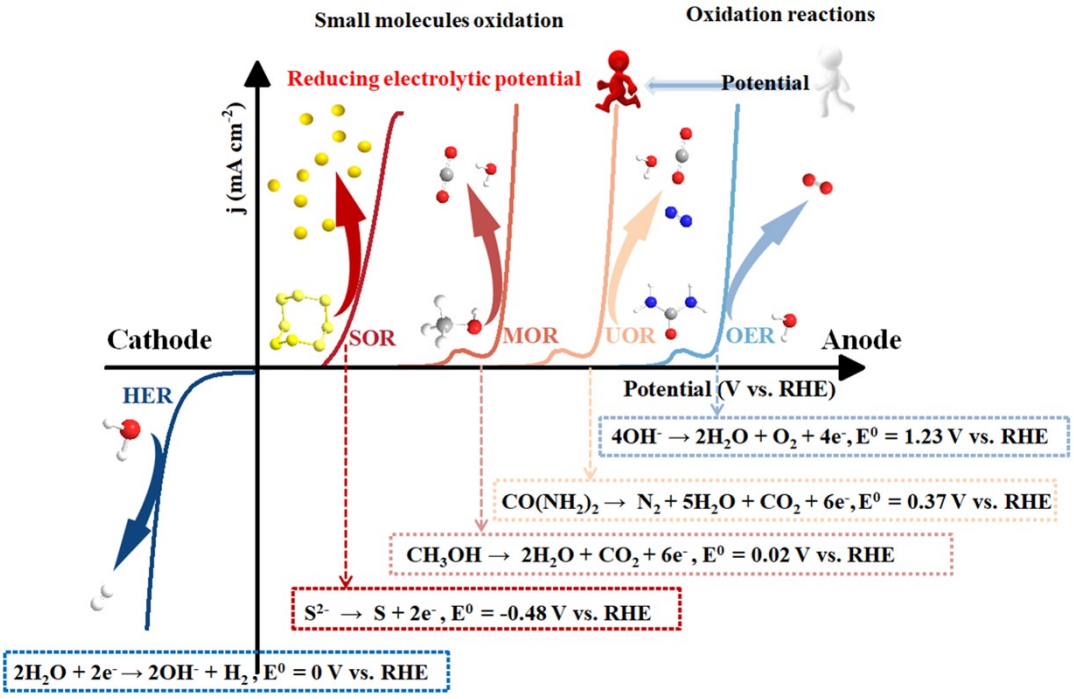

Fig. S1. Schematic diagram of small molecule oxidation.

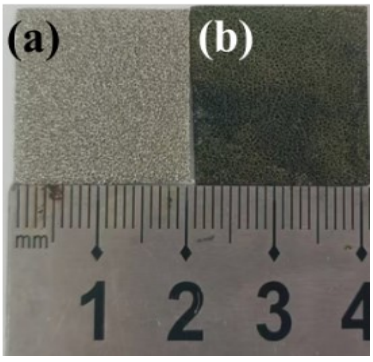

Fig. S2. Photograph of the fabricated electrodes of (a) NF and (b) FeCoNiMnMg-S.

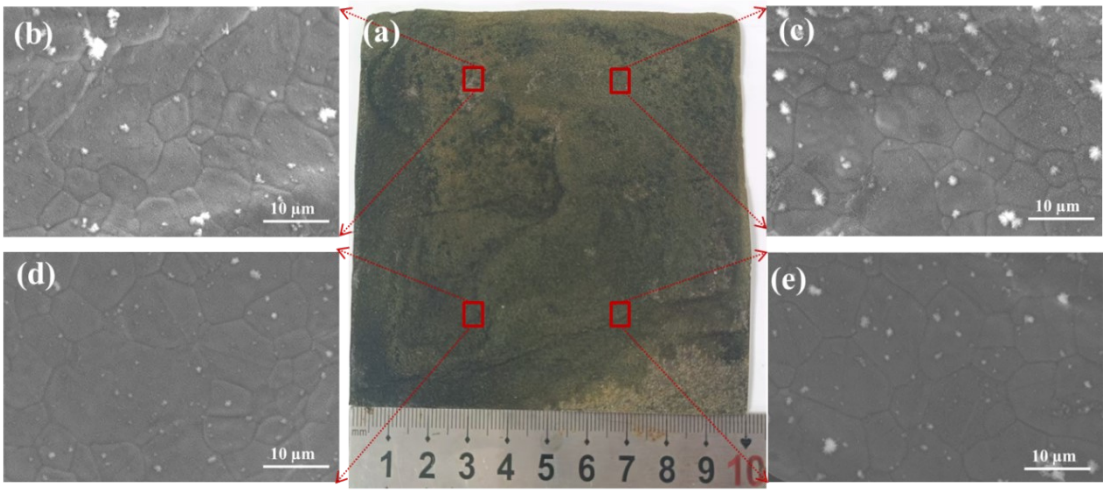

Fig. S3. (a) Optical-photo image of large size NF corrosion treatment, (b-e) SEM images of FeCoNiMnMg-S taken from different sections (marked in Figure S3a).

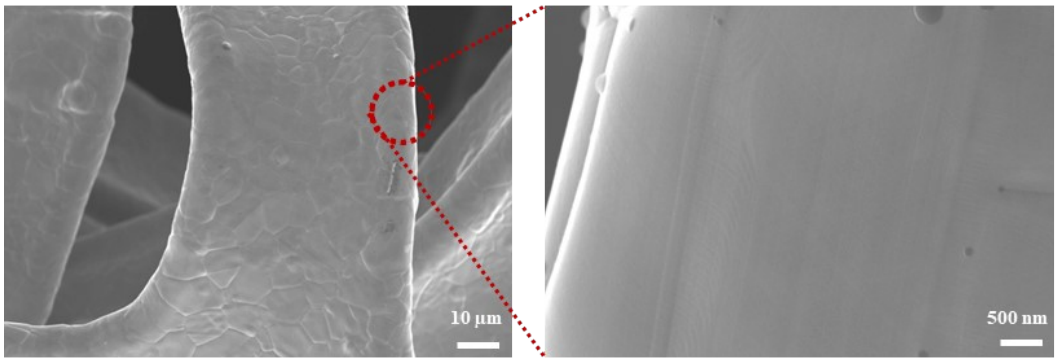

Fig. S4. SEM images of bare Ni foam.

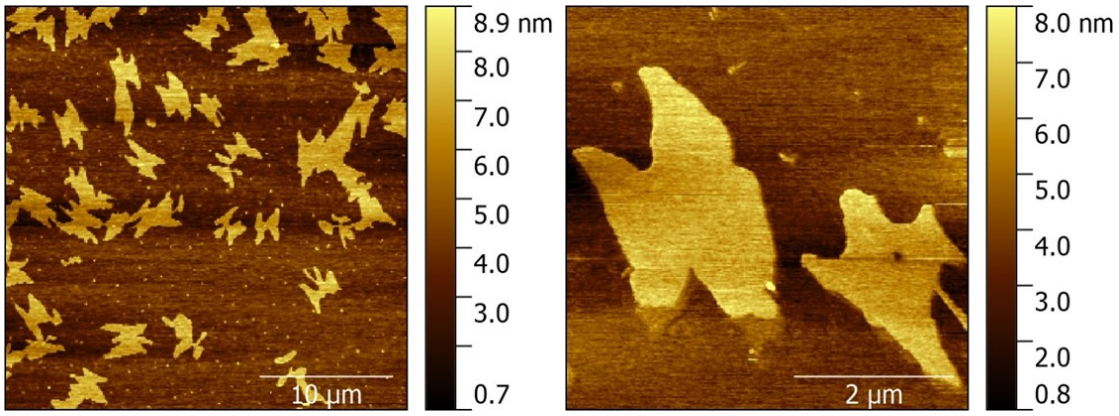

Fig. S5. AFM images of FeCoNiMnMg-S.

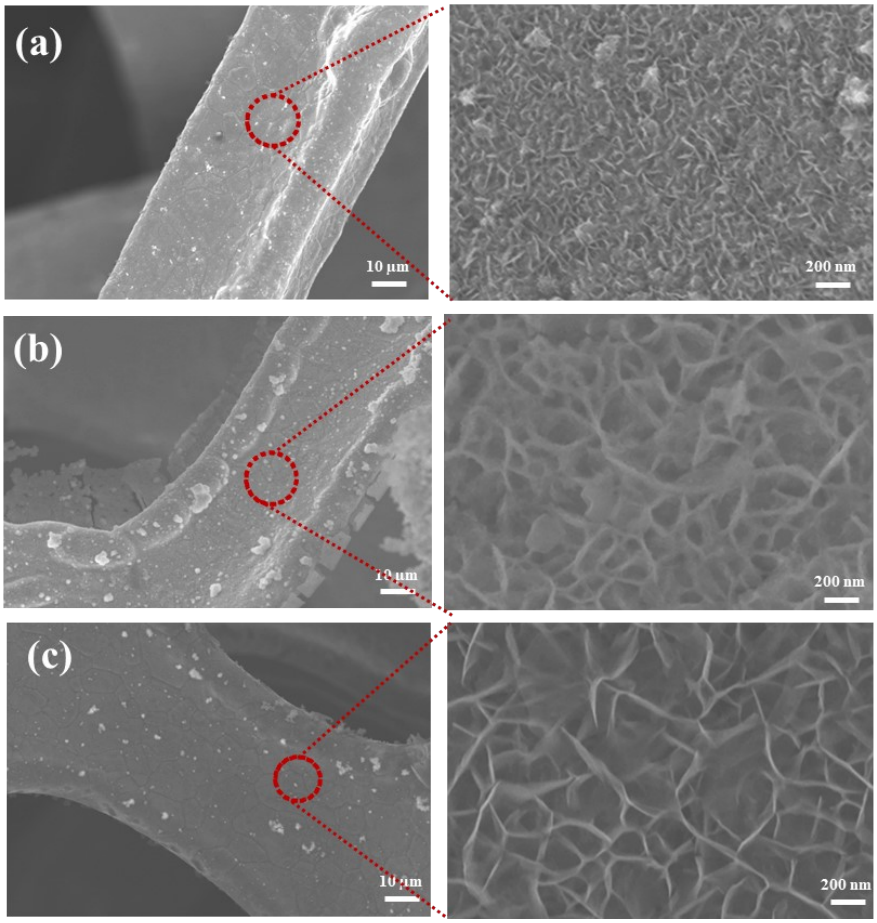

Fig. S6. SEM images of the (a) FeCoNi-S, (b) FeCoNiMg-S and (c) FeCoNiMnMg-S.

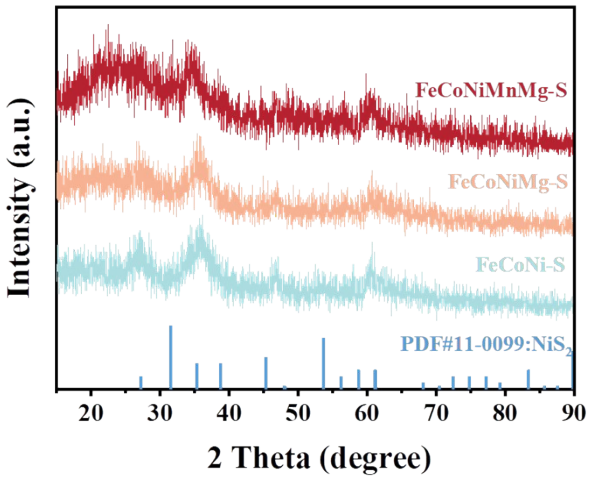

Fig. S7. XRD patterns of FeCoNi-S, FeCoNiMg-S and FeCoNiMnMg-S after removing NF.

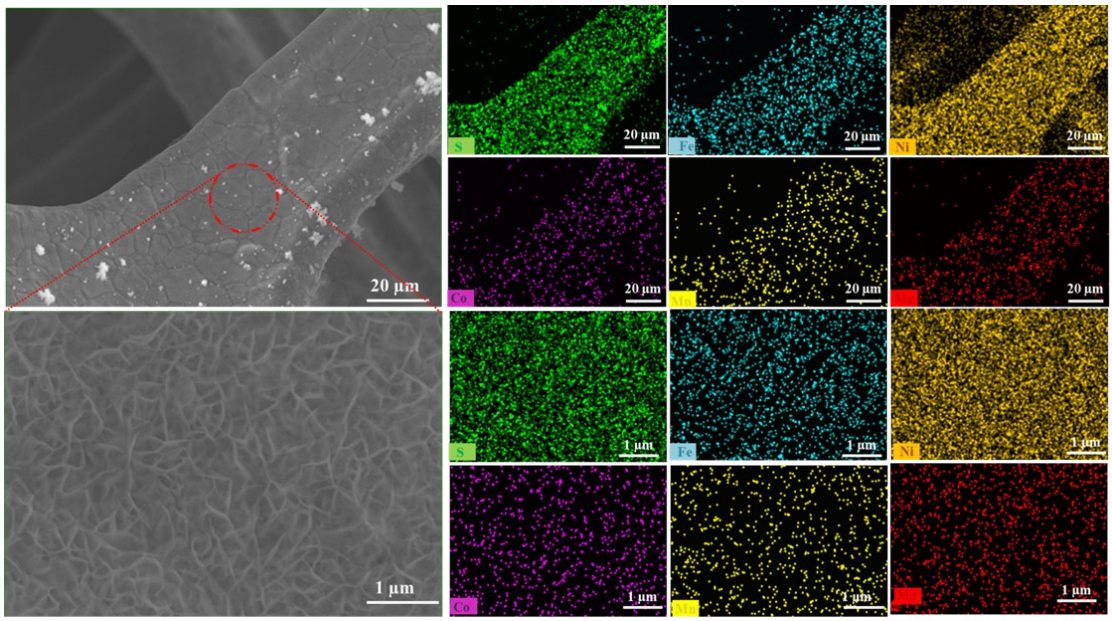

Fig. S8. SEM and corresponding EDX element mapping images of the FeCoNiMnMg-S.

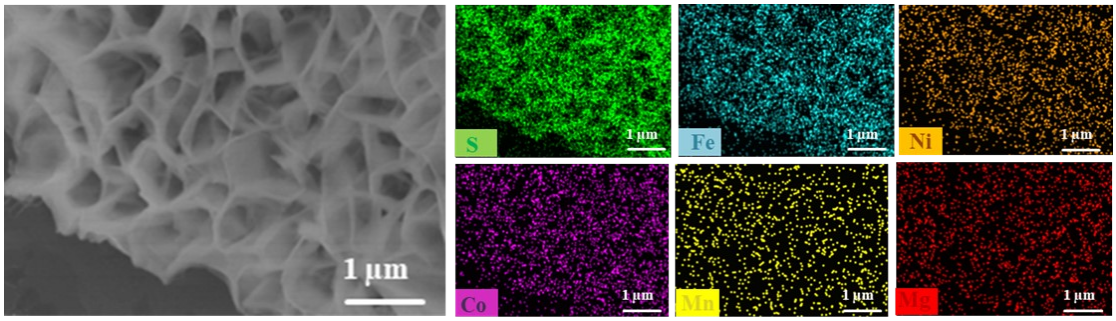

Fig. S9. SEM and corresponding EDX element mapping images of the FeCoNiMnMg-S (Nanosheets sonicated from nickel foam substrates).

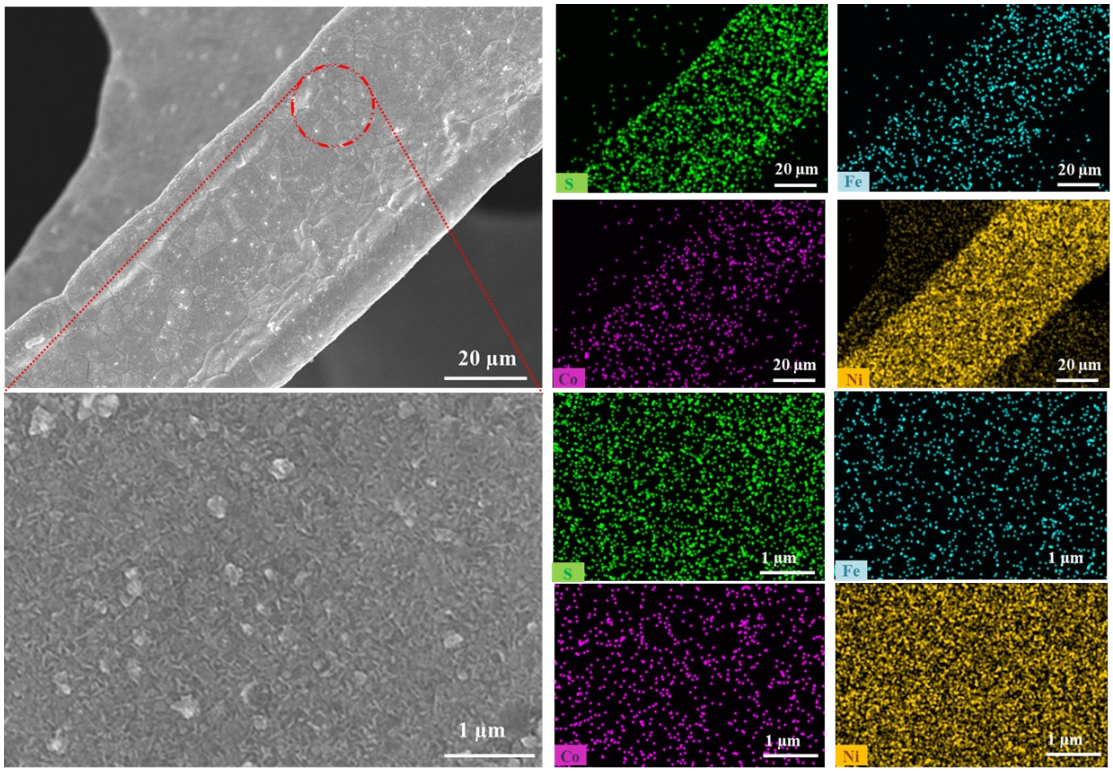

Fig. S10. SEM and corresponding EDX element mapping images of the FeCoNi-S.

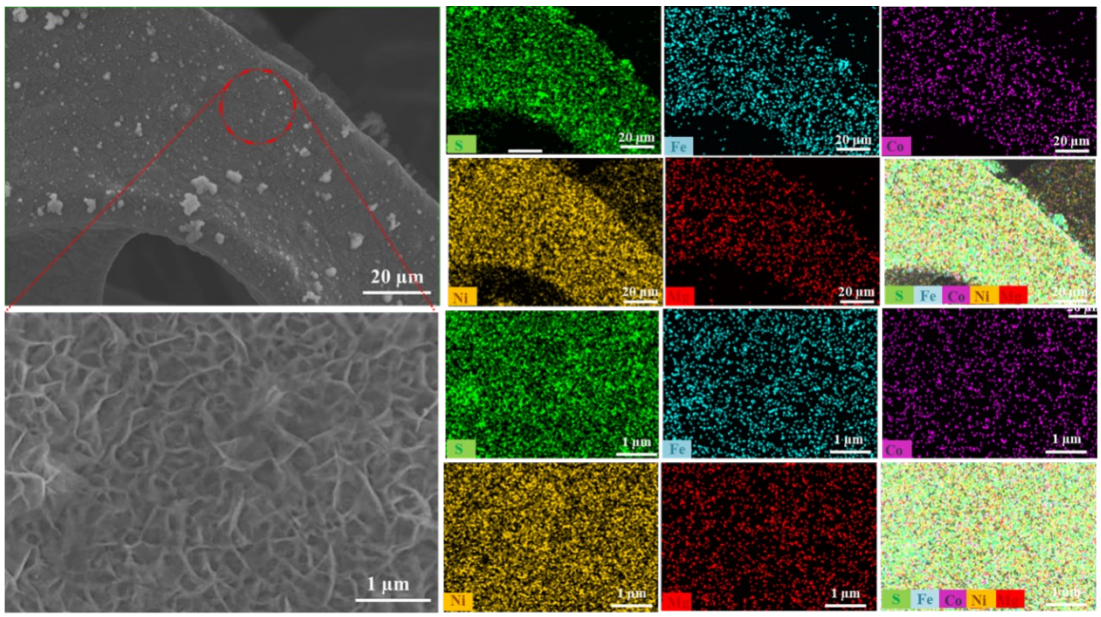

Fig. S11. SEM and corresponding EDX element mapping images of the FeCoNiMg-S.

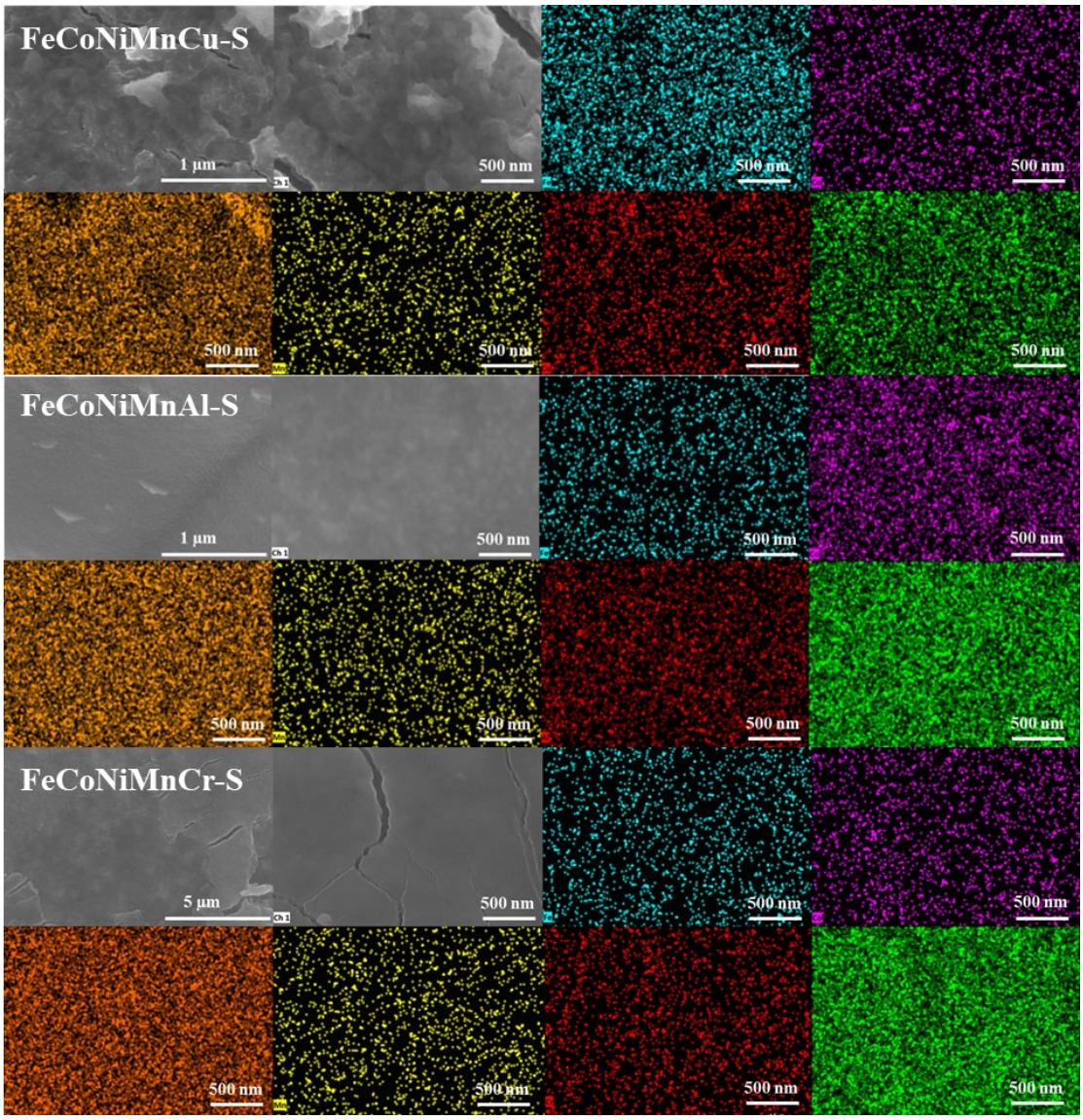

Fig. S12. SEM and corresponding EDX element mapping images of the FeCoNiMnAl-S, FeCoNiMnCu-S and FeCoNiMnCr-S.

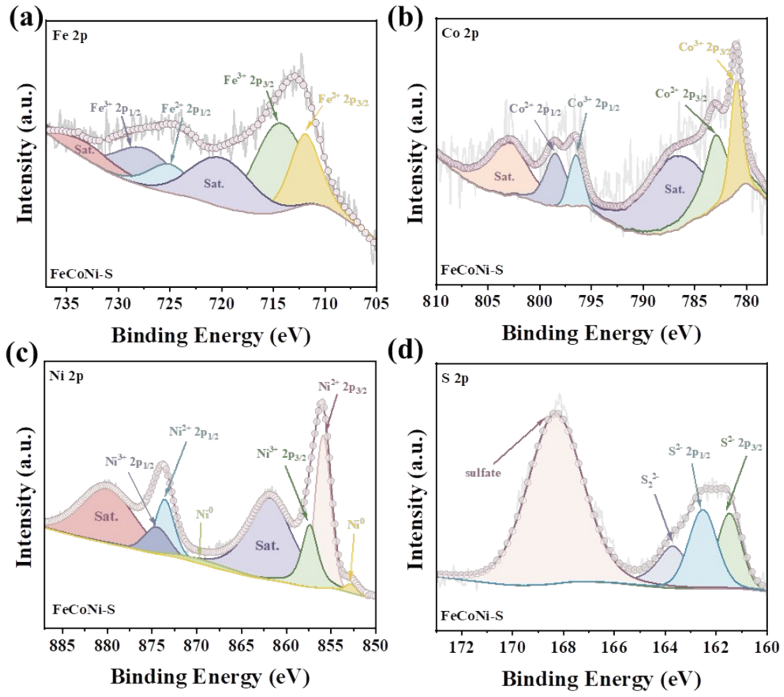

Fig. S13. High resolution XPS spectra of (a) Fe 2p, (b) Co 2p, (c) Ni 2p and (d) S 2p in FeCoNi-S.

XPS survey spectra revealed that the presence of Fe, Co, Ni, S and O elements in the FeCoNi-S. The XPS spectrum of FeCoNi-S is shown in **Fig. S13**, where the Fe 2p spectrum is divided into Fe $2p_{1/2}$ and Fe $2p_{3/2}$, the peaks near 711.9 eV (Fe $2p_{3/2}$) and 725.1 eV (Fe $2p_{1/2}$) correspond to Fe^{2+}, while the peaks at 714.4 eV (Fe $2p_{3/2}$) and 728.3 eV (Fe $2p_{1/2}$) are attributed to the presence of Fe^{3+}. **Fig. S13b** shows the XPS spectrum of Co 2 p, where the Co $2p_{3/2}$ (Co^{2+}/Co^{3+}) peak is deconvoluted into two peaks at 782.9 and 781.0 eV, the Co $2p_{1/2}$ (Co^{2+}/Co^{3+}) peak is located at 798.5 and 796.5 eV, and the two peaks at 786.8 and 803.1 eV are satellite peaks. Similarly, **Fig. S13c** shows the XPS spectrum of Ni 2p, where the peaks at 855.9 eV (Ni $2p_{3/2}$) and 873.6 eV (Ni $2p_{1/2}$) confirm the presence of Ni^{2+}, while the peaks near 857.5 eV (Ni $2p_{3/2}$) and 874.6 eV (Ni $2p_{1/2}$) indicate the presence of Ni^{3+}. Additionally, the two small peaks at 870.2 eV and 852.9 eV belong to Ni^{0}, while the peaks near 861.9 and 880.3 eV correspond to the two satellite peaks of Ni.

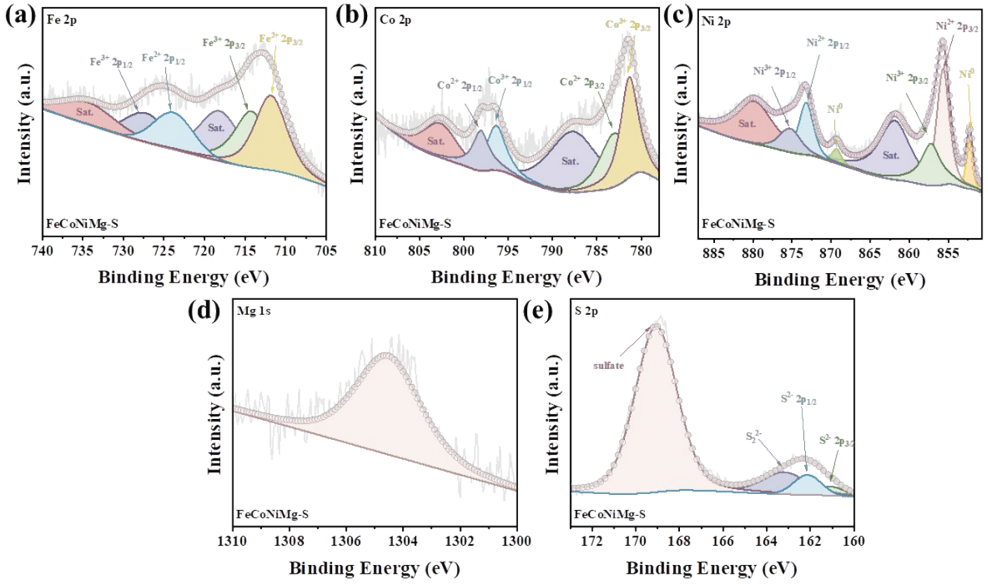

Fig. S14. XPS spectra of (a) Fe 2p, (b) Co 2p, (c) Ni 2p, (d) Mg 2p and (e) S 2p in FeCoNiMg-S.

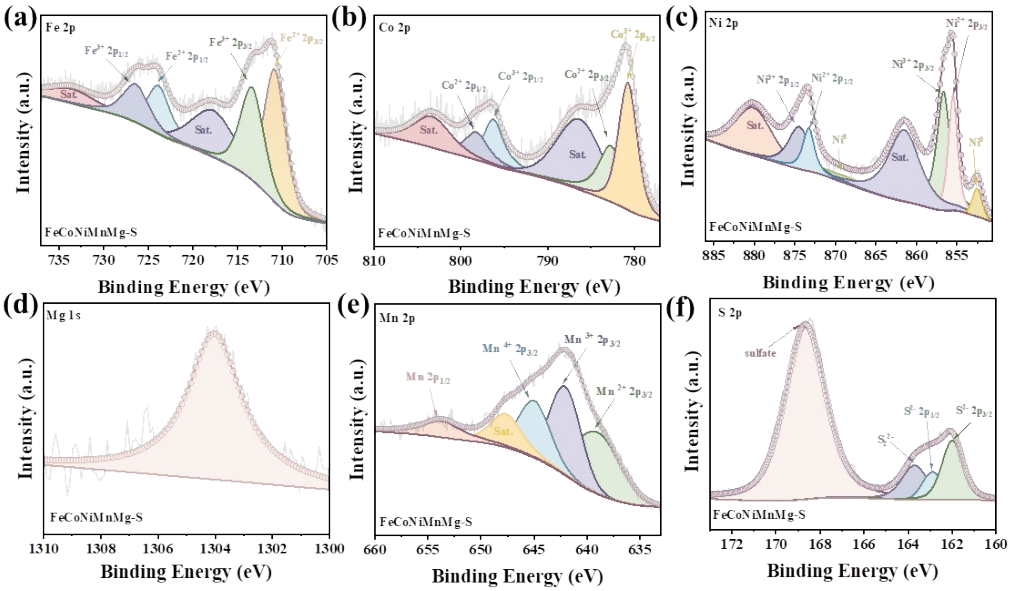

Fig. S15. XPS spectra of (a) Fe 2p, (b) Co 2p, (c) Ni 2p, (d) Mg 2p, (e) Mn 2p and (f) S 2p in FeCoNiMnMg-S.

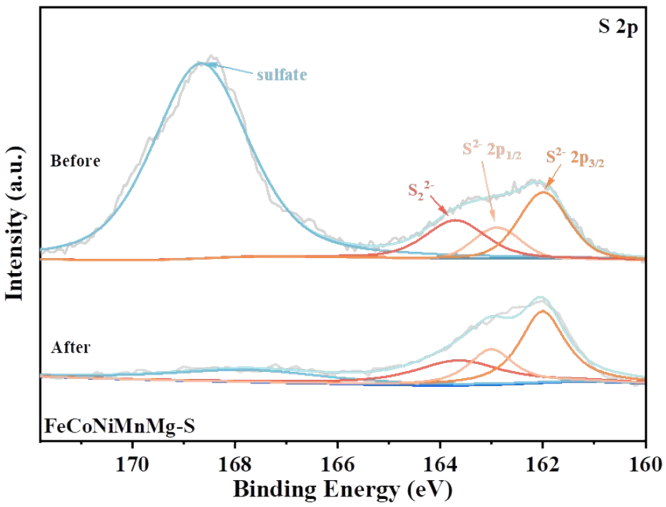

Fig. S16. XPS comparison diagram of the FeCoNiMnMg-S before and after Ar^+ etching.

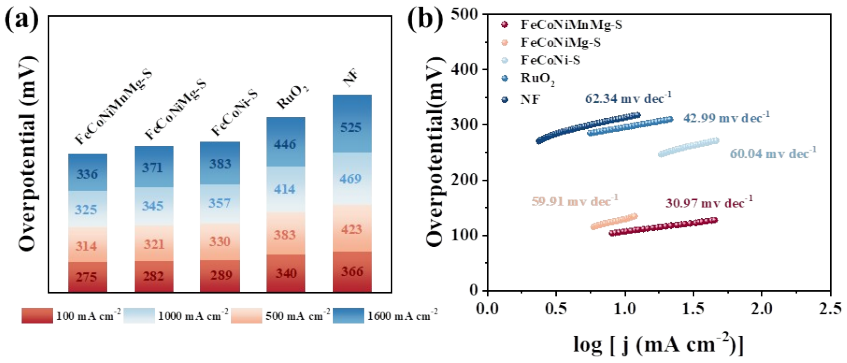

Fig. S17. (a) The overpotential of the prepared catalyst at current densities of 100, 500, 1000 and 1600 mA cm^{-2}. (b) Tafel curves calculated from OER polarization curves.

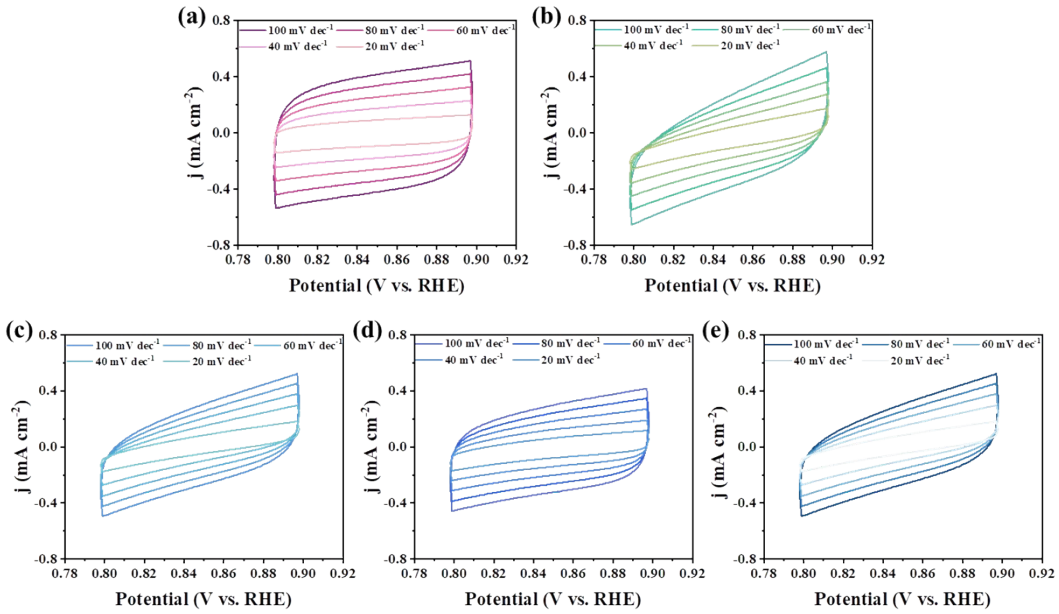

Fig. S18. CV curves of the (a) FeCoNiMnMg-S, (b) FeCoNiMg-S, (c) FeCoNi-S, (d) RuO_2 and (e) NF at different scanning rates.

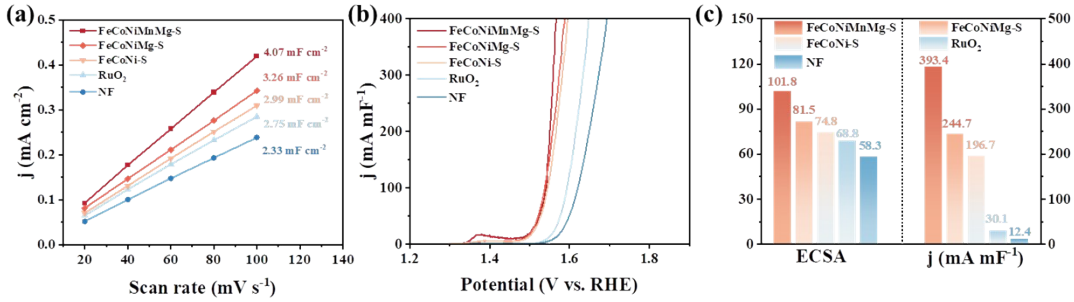

Fig. S19. (a) The corresponding C_{dl} of the catalysts, (b) Normalized current density, (c) The ECSA and the normalized current collected at 1.55 V vs. RHE of the FeCoNiMnMg-S, FeCoNiMg-S, FeCoNi-S, RuO_2 and NF.

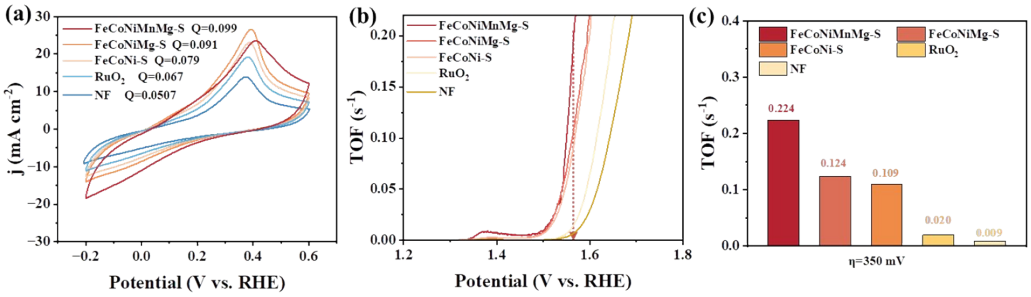

Fig. S20. (a) CV curves for recorded between –0.2 V to 0.6 V vs. RHE in 1.0 M phosphate buffer saline (PBS, pH = 7) at a scan rate of 50 mV s^{-1}. (b) The TOF curves of FeCoNiMnMg-S, FeCoNiMg-S, FeCoNi-S, RuO_2 and NF in OER process, and (c) TOF values of the catalyst at η=350 mV.

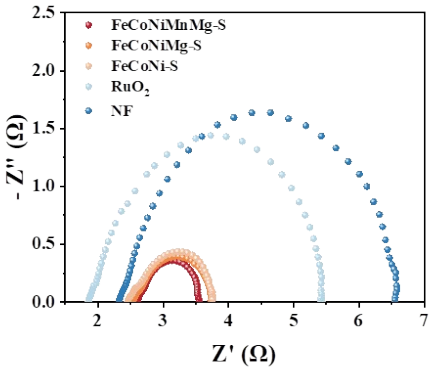

Fig. S21. Nyquist plots of the electrodes measured at a voltage of 1.56 V vs. RHE over the frequency range of 10^5 - 0.1 Hz of the FeCoNiMnMg-S, FeCoNiMg-S, FeCoNi-OH, RuO_2 and NF.

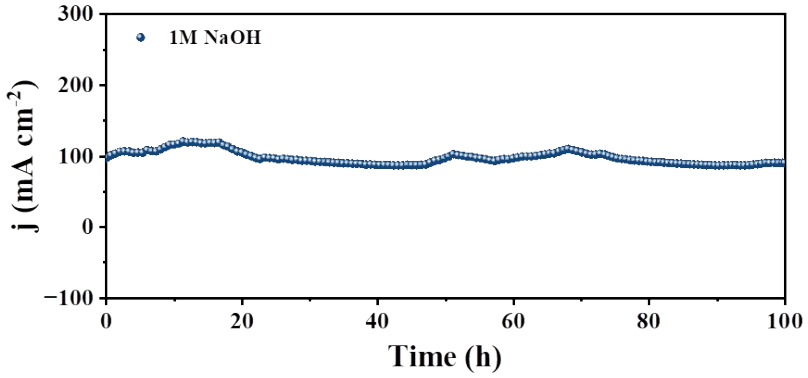

Fig. S22. Stability test of FeCoNiMnMg-S in 1.0 M NaOH for 100 h.

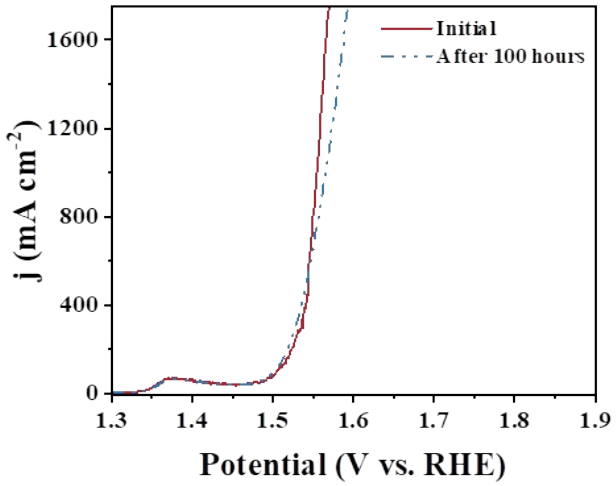

Fig. S23. LSV curves of the FeCoNiMnMg-S before and after the 100 h stability test.

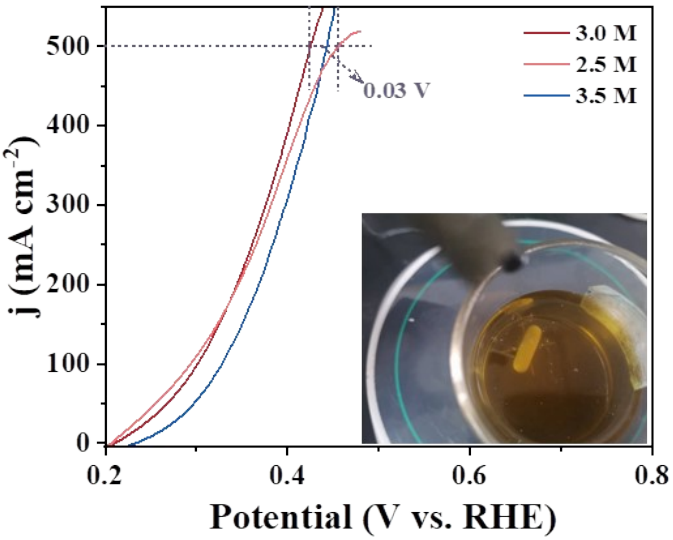

Fig. S24. SOR polarization curves of FeCoNiMnMg-S in 1.0 M NaOH solutions containing different Na_2S concentrations (2.5 - 3.5 M); Inset: Optical photograph of the reaction tank after testing in 1.0 M NaOH + 3.5 M Na_2S solution.

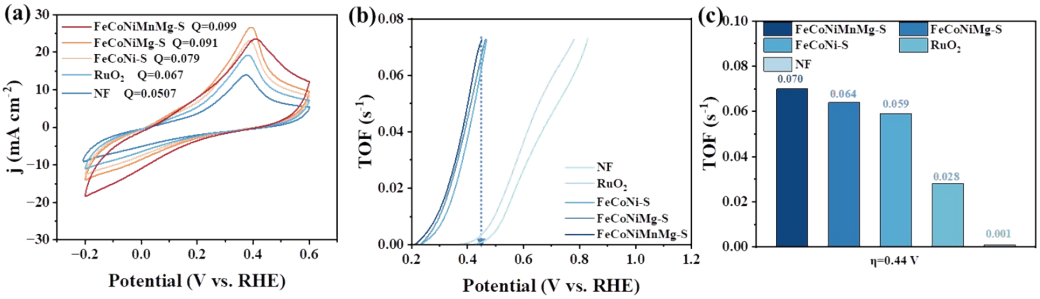

Fig. S25. (a) CV curves for recorded between –0.2 V to 0.6 V vs. RHE in 1.0 M phosphate buffer saline (PBS, pH = 7) at a scan rate of 50 mV s^{-1}. (b) The TOF curves of FeCoNiMnMg-S, FeCoNiMg-S, FeCoNi-S, RuO_2 and NF in SOR process, and (c) TOF values of the catalyst at η=0.44 V.

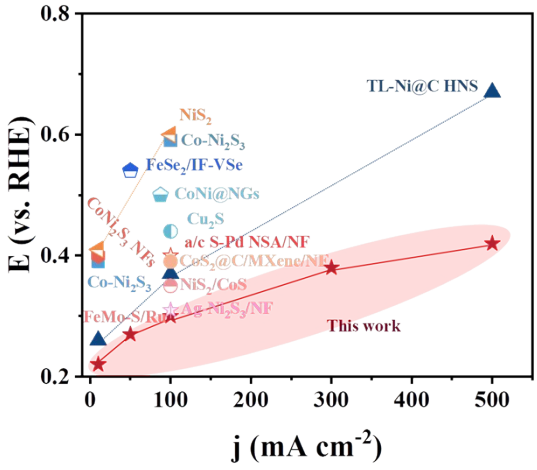

Fig. S26. The SOR performance comparison between FeCoNiMnMg-S and other reported materials.

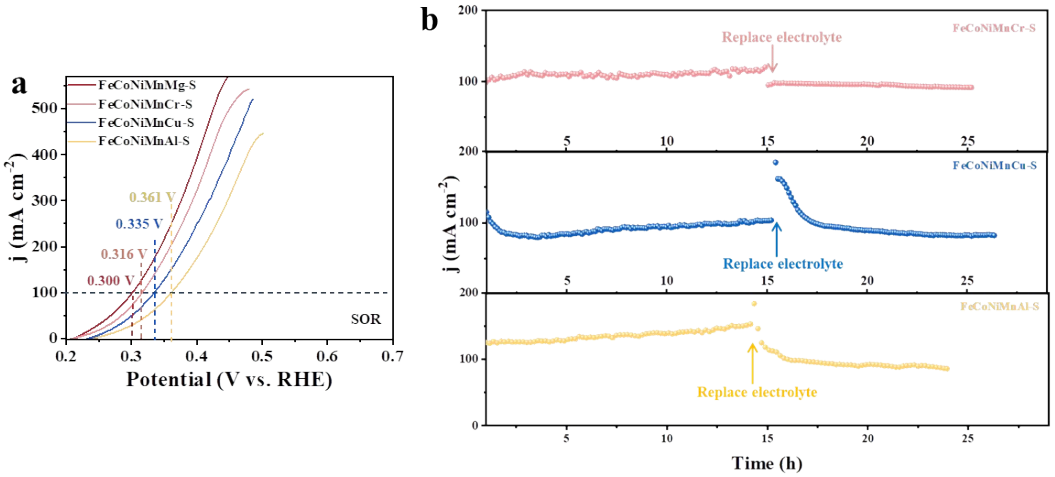

Fig. S27. (a) Current density of FeCoNiMnMg-S, FeCoNiMnAl-S, FeCoNiMnCr-S, and FeCoNiMnCu-S in SOR, (b) Catalyst's SOR stability test comparison.

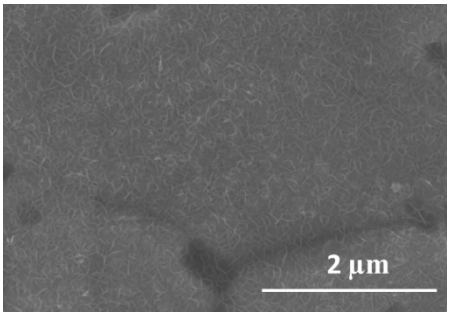

Fig. S28. SEM image of FeCoNiMnMg-S after reaction in 1.0 M NaOH + 3.0 M Na_2S.

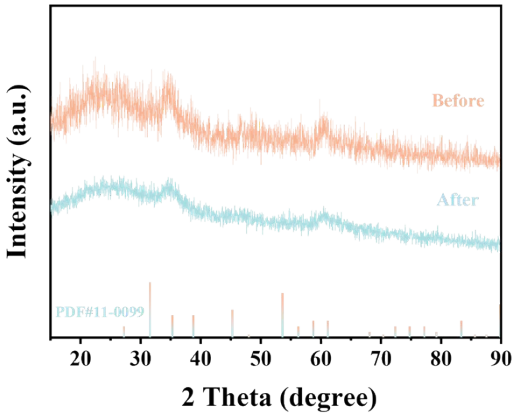

Fig. S29. XRD patterns after removing NF. The XRD pattern of FeCoNiMnMg-S after the stability reaction.

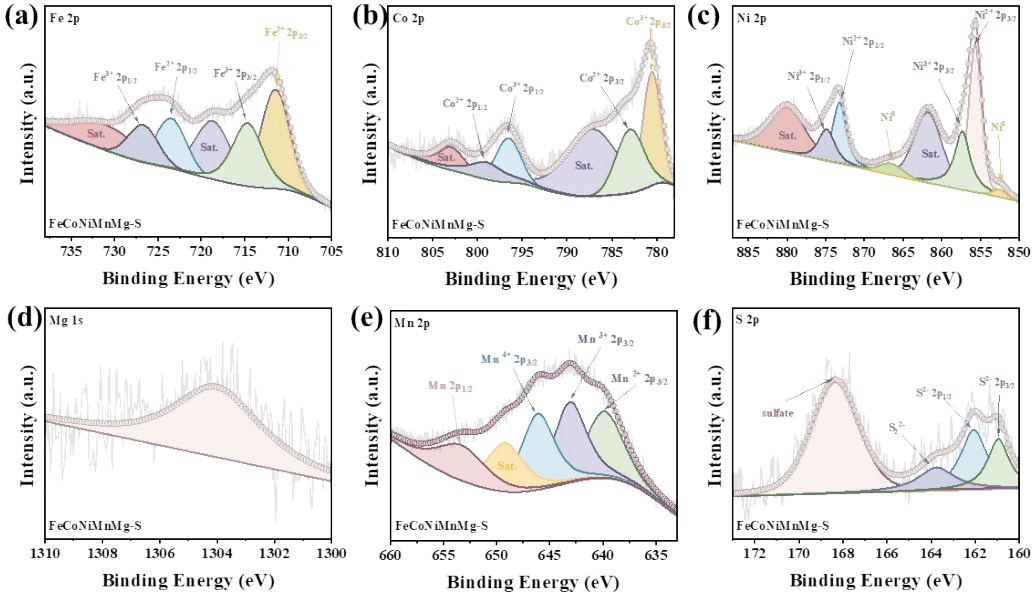

Fig. S30. XPS spectra of (a) Fe 2p, (b) Co 2p, (c) Ni 2p, (d) Mg 2p, (e) Mn 2p and (f) S 2p in FeCoNiMnMg-S after the stability test.

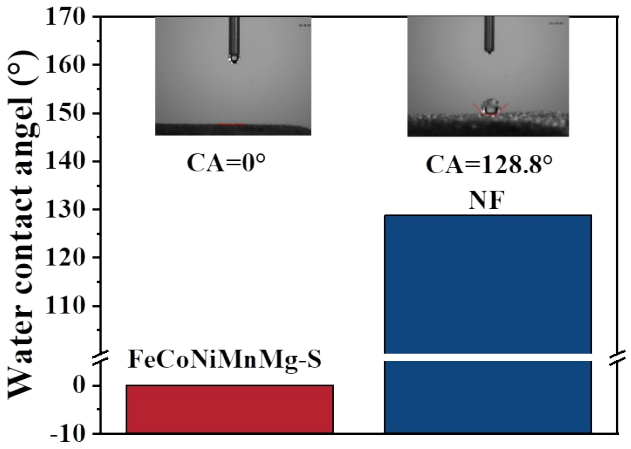

Fig. S31. Water contact angles on (a) FeCoNiMnMg-S and (b) NF electrode.

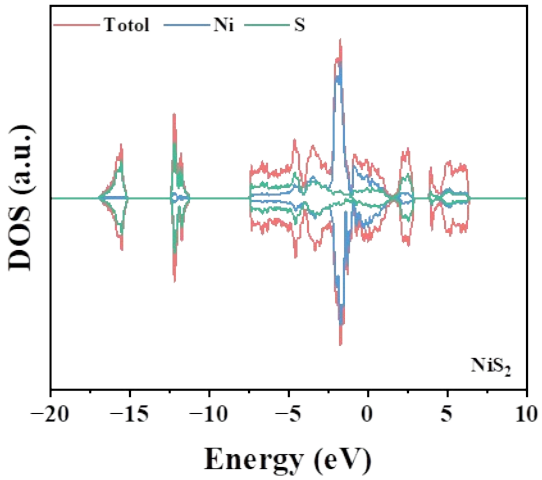

Fig. S32. The density of states of NiS_2.

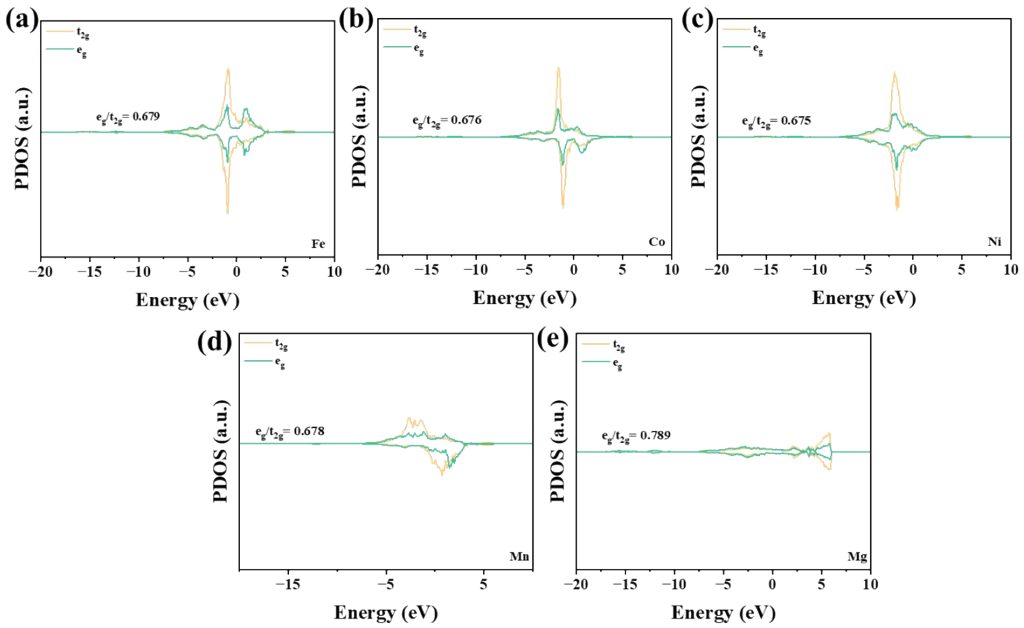

Fig. S33. (a-e) Projected PDOS plots for different orbitals for Fe, Co, Ni, Mn and Mg catalysts (top to bottom).

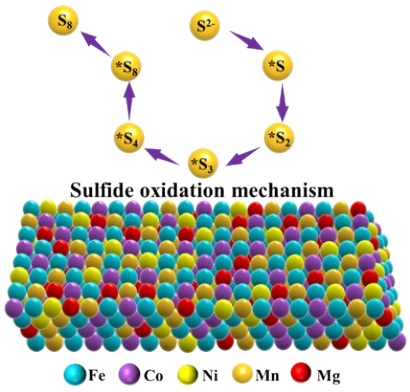

Fig. S34. Mechanistic diagram illustrating the catalytic process of FeCoNiMnMg-S for SOR.

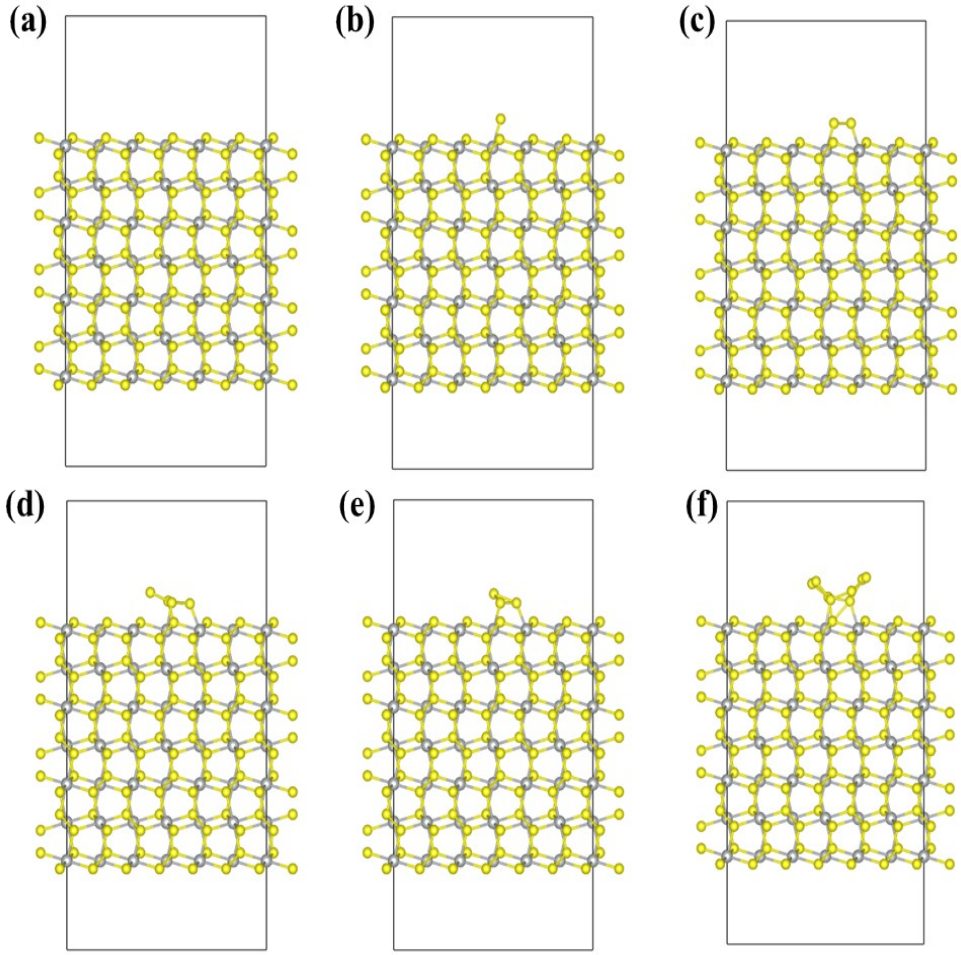

Fig. S35. (a-f) The adsorption structure of *S, *S_2, *S_3, *S_4 and *S_8 intermediates on NiS_2. Gray and yellow spheres represent Ni and S atoms, respectively.

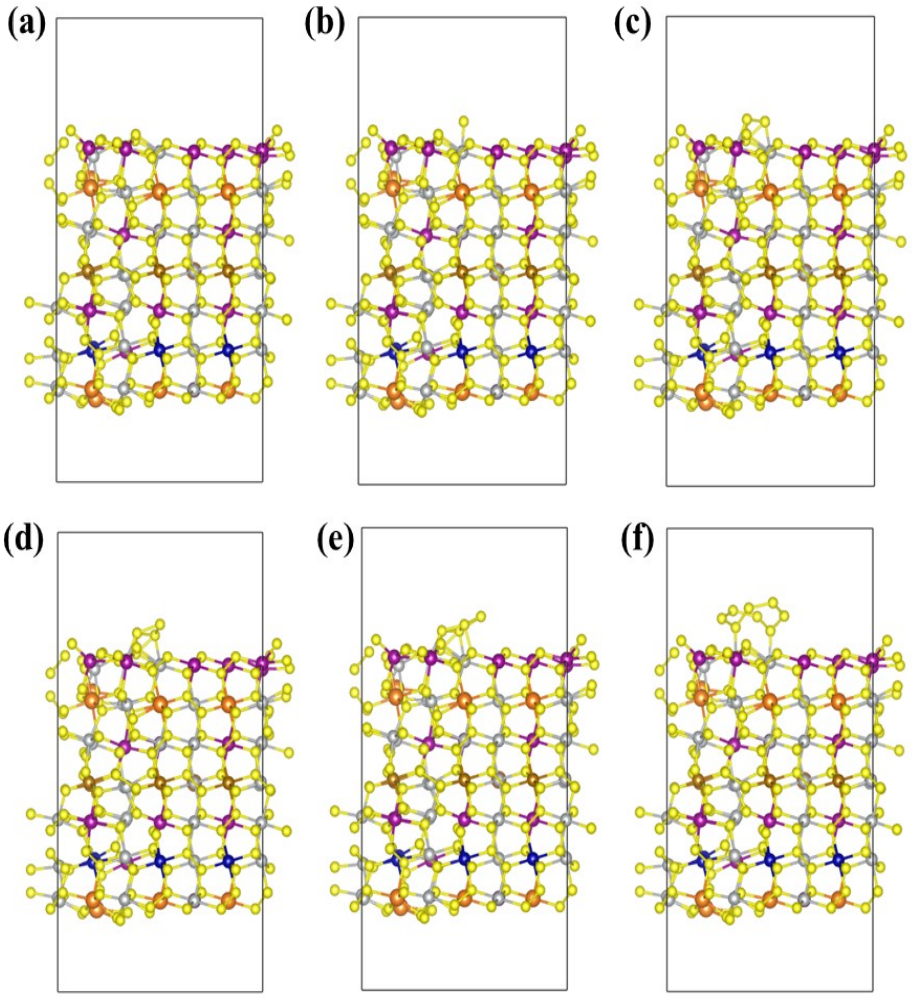

Fig. S36. (a-f) The adsorption structure of *S, *S_2, *S_3, *S_4 and *S_8 intermediates on FeCoNiMnMg-S. Gray, orange, brown, cyan, purple and yellow spheres represent Ni, Mg, Fe, Co, Mn and S atoms, respectively.

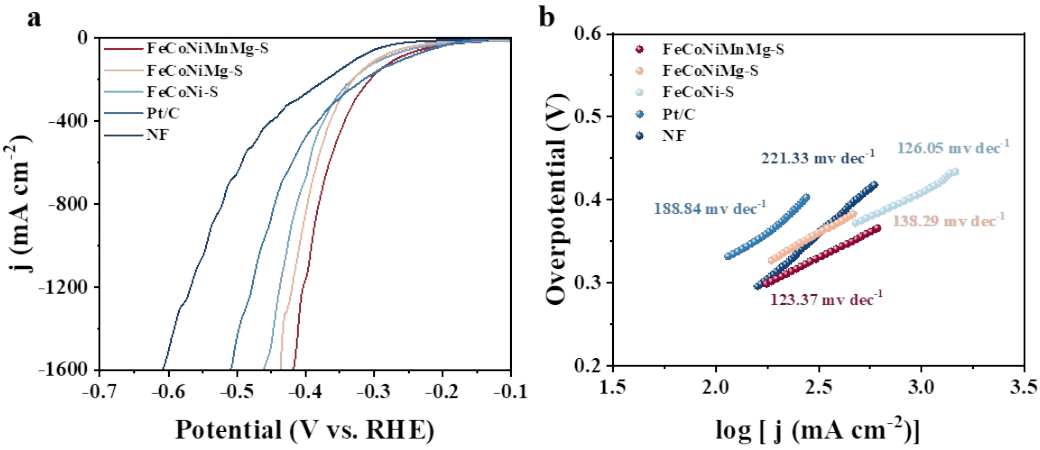

Fig. S37. (a) HER polarization curves of prepared catalysts, (b) Tafel plots calculated from HER polarization curves.

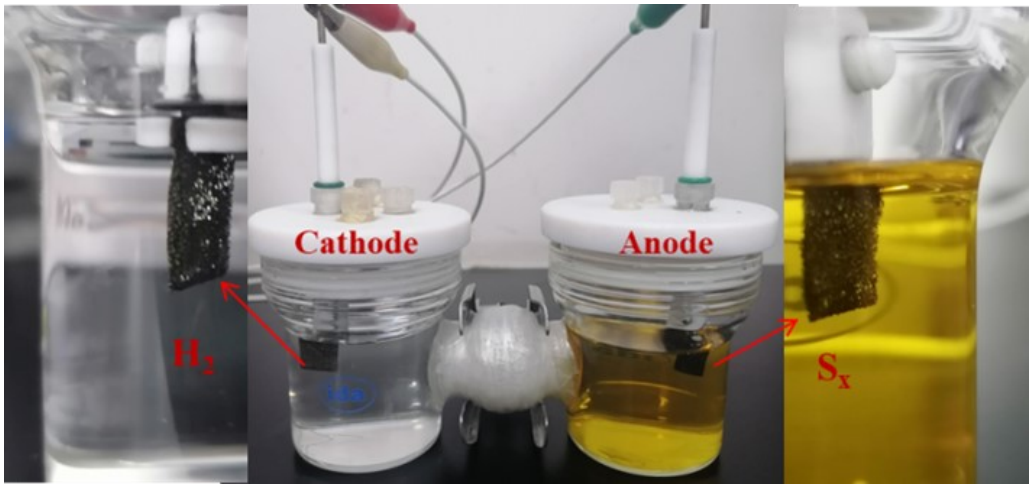

Fig. S38. Digital image of the electrocatalytic coupling system using bifunctional FeCoNiMnMg-S electrodes in 1.0 M NaOH for HER (left) and in 1.0 M NaOH + 3 M Na_2S for SOR (right).

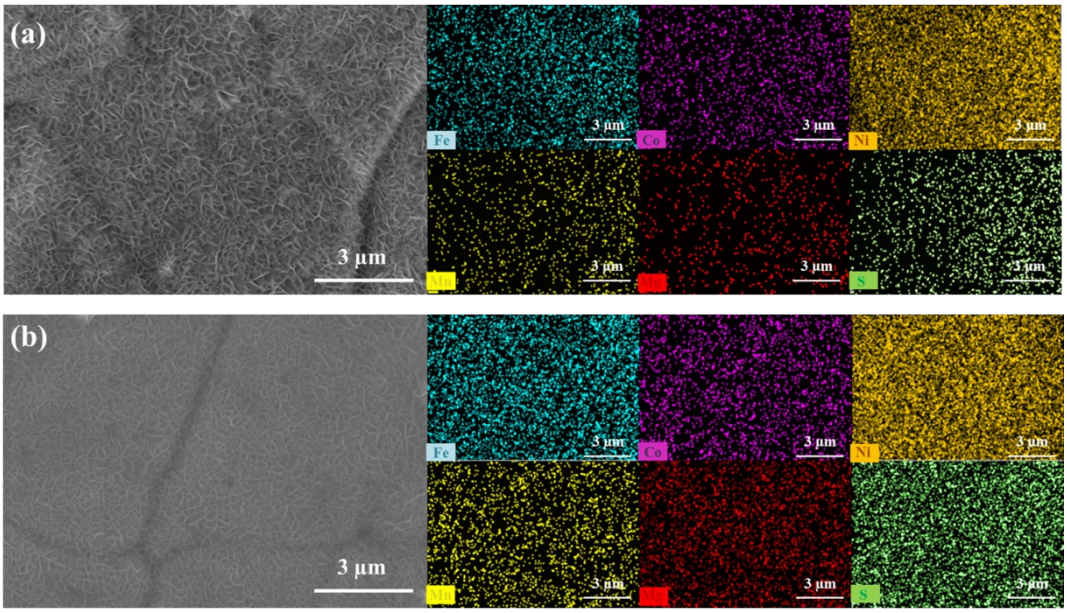

Fig. S39. (a) SEM image and SEM-EDS elemental mapping of FeCoNiMnMg-S after reaction in anode electrolyte, (b) SEM image and SEM-EDS elemental mapping of FeCoNiMnMg-S after reaction in cathode electrolyte.

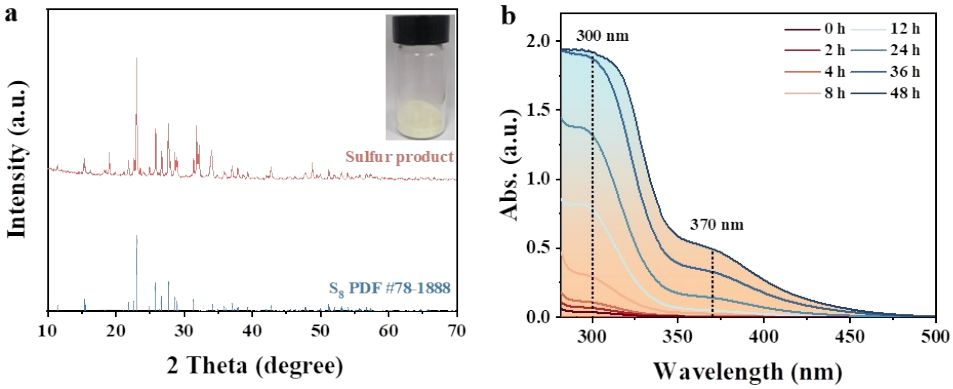

Fig. S40. (a) XRD pattern of product S, the inset photo is the collected product of S powder. (b) The UV-vis spectra of the anolyte diluted 250 times at 100 mA cm^{-2}.

Table S1. ICP-OES of FeCoNiMnMg-S.

Element	Fe	Co	Ni	Mn	Mg	S
Mass fraction (%)	13.82	13.13	16.24	12.32	5.81	38.68

Table S2. Comparison of the OER performances with previously reported electrocatalysts in 1.0 M NaOH/KOH.

Catalyst	Tafel slope (mV dec^{-1})	η_{100}(mV)	Durability (h @ mA cm^{-2})	Ref.
FeCoNiMnMg-S	**30.97**	**275**	**100 @ 100**	**This work**
$CrMnFeCoNiS_{0.3}$	32.30	285	100 @ 10	[5]
NiCoFeCuS	57.97	321	24 @ 100	[6]
$(CoFeNiMnCu)S_2$	57.00	370	2 @ 100	[7]
$(NiFeCoMn)_3S_4$	75.60	320	48 @ 10	[8]
FeCoNiCuAlV-S4	120.00	500	10 @ 20	[9]
NiFeCoMnAl	47.62	300	50 @ 10	[10]
$Fe_{1.2}(CoNi)_{1.8}S_6$	53.00	276	24 @ 200	[11]
NiFeS@NF	34.80	360	12 @ 100	[12]
FeS-NiS/NF	142.70	333	60 @ 100	[13]
CuCrFeNiCoP	70.70	423	24 @ 100	[14]
CoNiFeMnPO	44.30	383	30 @ 50	[15]
FeNiCoCrMn-G	40.00	278	36 @ 100	[16]
$(MgMnFeCoNi)S_x$	56.20	320	120 @ 10	[17]
$(FeCoNiMnMo)S_x$	66.60	390	100 @ 10	[18]
a-NiCoFeOS/c-CeO_2	80.56	350	100 @ 50	[19]

Table S3. A comparison of FeCoNiMnMg-S with reported electrodes in SOR performance.

Catalyst	Tafel slope ($mV\ dec^{-1}$)	Potential (V @ $mA\ cm^{-2}$)	Durability (h @ $mA\ cm^{-2}$)	Electrolyte	Ref.
FeCoNiMnMg-S	**22.02**	**0.22 @ 10 0.30 @ 100 0.42 @ 500**	**100 @ 100**	**1.0 M NaOH + 3.0 M Na_2S**	**This work**
FeMo-S/Ru	14.7	0.30 @ 100	50 @ 10	1.0 M NaOH + 1.0 M Na_2S	20
CoNi@NGs	/	0.50 @ 87.44	500 @ 30	1.0 M NaOH + 1.0 M Na_2S	21
a/c S-Pd NSA/NF	/	0.40 @ 100	20 @ 10	1.0 M KOH + 3.0 M Na_2S	22
Co-Ni_3S_2	176.4	0.39 @ 10 0.59 @ 100	24 @ 50	1.0 M NaOH + 1.0 M Na_2S	23
TL-Ni@C HNS	102.3	0.26 @ 10 0.37 @ 100 0.67 @ 500	/	1.0 M NaOH + 0.8 M Na_2S	24
$CoNi_2S_4$ NFs	124.1	0.40 @ 10	20 @ 10	1.0 M NaOH + 1.0 M Na_2S	25
NiS_2	104.0	0.41 @ 10 0.60 @ 100	4 @ 20	1.0 M NaOH + 0.05 M Na_2S	26
Cu_2S	68.0	0.44 @ 100	48 @ 50	1.0 M NaOH + 1.0 M Na_2S	27
CoS_2@C/MXene/NF	/	0.39 @ 100	240 @ 300	1.0 M NaOH + 1.0 M Na_2S	28
NiS_2/CoS	95.72	0.35 @ 100	25 @ 100	1.0 M NaOH + 1.0 M Na_2S	29
$FeSe_2$/IF-VSe	105.9	0.54 @ 50	120 @ 50	1.0 M NaOH + 1.0 M Na_2S	30
Ag-Ni_3S_2/NF	18.9	0.31 @ 100	20 @ 10	1.0 M KOH + 1.0 M Na_2S	31

Table S4. T The performance of the electrocatalytic coupling system (HER+SOR) for FeCoNiMnMg-S || FeCoNiMnMg-S compared with recently reported coupled catalysts.

Catalyst	Cell voltage (V @ mA cm^{-2})	Stability (h)	Reference
FeCoNiMnMg-S	0.74 @ 100	**200**	**This work**
Cu_2S	0.5 @ 10	144	[27]
Co-Ni_3S_2-2	0.79 @ 100	24	[23]
$CoNi_2S_4$ NFs	1.3 @ 40	144	[25]
a/c S-Pd NSA/NF	0.63 @ 100	120	[22]
CoS_2/MoS_2	1.29 @ 10	60	[32]
CuCoNiMnCrSx/NF ||Pt-CuCoNiSx/NF	0.73 @ 200	192	[33]
Co_3S_4	0.50 @ 100	25	[34]
$FeSe_2$/IF-VSe	1.05 @ 100	72	[30]
CuCoN/CC||CuCoS/CC	0.75 @ 100	144	[35]

References

1. G. Kresse, Phys. Rev. B, 1996, **54**, 11169-11186.
2. W. Kohn and L. J. Sham, Phy. Rev., 1965, **140**, A1133-A1138.
3. J. P. Perdew, J. A. Chevary, S. H. Vosko, K. A. Jackson, M. R. Pederson, D. J. Singh and C. Fiolhais, Phys. Rev. B, 1992, **46**, 6671-6687.
4. J. P. Perdew, K. Burke and M. Ernzerhof, Phys. Rev. Lett., 1996, **77**, 3865-3868.
5. D. Wang, C. Duan, Y. Yu, X. Li, Z. Wang, Y. Liu and C. Liu, J. Alloys Compd., 2023, **967**, 171758.
6. P. Yang, M. Sun, J. Wang, J. Li, R. Yang, Y. Hao, L. Qi, L. Yang and X. Liu, Particuology, 2024, **93**, 180-185.
7. M. Moradi, F. Hasanvandian, A. Bahadoran, A. Shokri, S. Zerangnasrabad and B. Kakavandi, Electrochim. Acta, 2022, **436**, 141444.
8. L. Wu, X. Shen, Z. Ji, J. Yuan, S. Yang, G. Zhu, L. Chen, L. Kong and H. Zhou, Adv. Funct. Mater., 2022, **33**, 2208170.
9. Y. Zhao, J. You, Z. Wang, G. Liu, X. Huang, M. Duan and H. Zhang, Int. J. Hydrogen Energy, 2024, **70**, 599-605.
10. M. Han, C. Wang, J. Zhong, J. Han, N. Wang, A. Seifitokaldani, Y. Yu, Y. Liu, X. Sun, A. Vomiero and H. Liang, Appl. Catal. B: Environ., 2022, **301**, 120764.
11. H. Wu, Z. Li, Z. Wang, Y. Ma, S. Huang, F. Ding, F. Li, Q. Zhai, Y. Ren, X. Zheng, Y. Yang, S. Tang, Y. Deng and X. Meng, Appl. Catal. B: Environ., 2023, **325**, 122356.
12. H. Fan, Y. Ma, W. Chen, Y. Tang, L. Li and J. Wang, J. Alloys Compd., 2022, **894**, 162533.
13. X. Wang, J. Zhang, M. Zhong, B. Su and Z. Lei, Int. J. Hydrogen Energy, 2024, **81**, 1209-1215.
14. T. Zhang, J. Li, B. Zhang, G. Wang, K. Jiang, Z. Zheng and J. Shen, J. Alloys Compd., 2023, **969**, 172439.
15. H.-M. Zhang, L. Zuo, Y. Gao, J. Guo, C. Zhu, J. Xu and J. Sun, J. Mater. Sci. Technol., 2024, **173**, 1-10.
16. T. X. Nguyen, Y. H. Su, C. C. Lin, J. Ruan and J. M. Ting, Adv. Sci., 2021, **8**, 2002446.
17. Y. Wang, H. Liu, J. Chen, K. Han, T. Xia, H. Yang, X. Yuan and Y. Zhao, J. Power Sources, 2025, **655**, 237936.
18. L. Bo, J. Fang, S. Yang, F. Nian, L. Pu, Z. Ma and J. Tong, Int. J. Hydrogen Energy, 2024, **84**, 89-96.
19. H.-M. Zhang, J. Li, M. Yao, Y. Li and J. Sun, Sci. Total Environ., 2025, **976**, 179330.
20. J. Wang, M. Zhou, R. Fu, J. Ge, W. Yang, X. Hong, C. Sun, X. Liao, Y. Zhao and Z. Wang, Adv. Funct. Mater., 2024, **34**, 2315326.
21. Mo Zhang, Jing Guan, Y. Tu, S. Chen, Y. Wang, S. Wang, L. Yu, C. Ma, D. Deng and X. Bao, Energy Environ. Sci., 2020, **13**, 119-126.
22. W. Wang, Q. Mao, K. Deng, H. Yu, Z. Wang, Y. Xu, X. Li, L. Wang and H. Wang, Small, 2023, **19**, 2207852.
23. Y. Li, Y. Duan, K. Zhang and W. Yu, Chem. Eng. J., 2022, **433**, 134472.

24. Y. Zhu, S. Wang, Y. Chen, Y. Zhang, Y. Feng and G. Zhang, Angew. Chem. Int. Ed., 2024, **64**, e202419572.
25. H. Wang, B. Wang, H. Yu, K. Deng, Y. Xu, X. Li, Z. Wang and L. Wang, ACS Appl. Nano Mater., 2023, **6**, 10863-10871.
26. S. Zhang, Q. Zhou, Z. Shen, X. Jin, Y. Zhang, M. Shi, J. Zhou, J. Liu, Z. Lu, Y. N. Zhou and H. Zhang, Adv. Funct. Mater., 2021, **31**, 2101922.
27. Y. Pei, J. Cheng, H. Zhong, Z. Pi, Y. Zhao and F. Jin, Green Chem., 2021, **23**, 6975-6983.
28. L. Zhang, Z. Wang and J. Qiu, Adv. Mater., 2022, **34**, 109321.
29. J. Huo, L. Jin, C. Chen, D. Chen, Z. Xu, C. D. Wilfred, Q. Xu and J. Lu, ACS Appl. Mater. Interfaces, 2023, **15**, 43976-43984.
30. X. Wang, J. Jiang, J. Zhang, Q. Zeng, A. Liu and L. Ai, J. Colloid Interface Sci., 2025, **684**, 367-376.
31. M. Ming, J. Kang, Y. Gu, J. Zhang, Q. Zhang, G. Fan and Q. Shen, J. Environ. Chem. Eng., 2025, **13**, 119139.
32. C. Li, Y. Liu, Z. Zhuo, H. Ju, D. Li, Y. Guo, X. Wu, H. Li and T. Zhai, Adv. Energy Mater., 2018, **8**, 1801775.
33. Y. Pei, D. Li, C. Qiu, L. Yan, Z. Li, Z. Yu, W. Fang, Y. Lu and B. Zhang, Angew. Chem. Int. Ed., 2024, **63**, e202411977.
34. Z. Xiao, C. Lu, J. Wang, Y. Qian, B. Wang, Q. Zhang, A. Tang and H. Yang, Adv. Funct. Mater., 2022, **33**, 2212183.
35. H. Yu, W. Wang, Q. Mao, K. Deng, Y. Xu, Z. Wang, X. Li, H. Wang and L. Wang, J. Mater. Chem. A, 2023, **11**, 2218-2224.